Scilight

Smart Chemical Engineering

https://www.sciltp.com/journals/sce

Article

Three-Dimensional Reconstruction of Fluidized Beds from Limited Measurements via a Physics Guided cGAN

Xue Li [1], Jie Xiang [2], Ting Zhang [2], Cheng Zhang [1], Anqi Li [3], Mao Ye [1,*] and Zhongmin Liu [1]

[1] National Engineering Research Center of Lower-Carbon Catalysis Technology, Dalian Institute of Chemical Physics, Chinese Academy of Sciences, Dalian 116023, China
[2] College of Computer Science and Technology, Shanghai University of Electric Power, Shanghai 200090, China
[3] School of Chemistry and Chemical Engineering, Chongqing University, Chongqing 400044, China
* Correspondence: maoye@dicp.ac.cn; Tel.: +86-0411-84379618

How To Cite: Li, X.; Xiang, J.; Zhang, T.; et al. Three-Dimensional Reconstruction of Fluidized Beds from Limited Measurements via a Physics Guided cGAN. *Smart Chemical Engineering* **2025**, *1*(1), 2. https://doi.org/10.53941/sce.2025.100002

Received: 4 August 2025
Revised: 2 September 2025
Accepted: 28 September 2025
Published: 23 October 2025

Abstract: Characterizing multiphase flows in fluidized beds remains challenging due to complex hydrodynamics, harsh operating conditions, and sensor limitations that restrict data acquisition. A physics guided conditional Generative Adversarial Network (PG-cGAN) framework is designed to reconstruct detailed three-dimensional (3D) fields from limited measurements. This hybrid approach integrates a gap-filling preprocess to mitigate data incompleteness, employs a multiscale strategy to enhance feature extraction from sparse inputs, and incorporates empirical correlations as physical constraints to ensure realistic reconstructions. Validation against computational fluid dynamics (CFD) simulations demonstrates close agreement between reconstructed and ground-truth fields. Furthermore, application of the PG-cGAN to 2D cross-sectional slices obtained from mobile Electrical Capacitance Tomography (ECT) experiments enables 3D fluidization analysis. The PG-cGAN framework provides potential for online characterization of complex flows by enabling rapid reconstruction from limited data.

Keywords: fluidized beds; conditional Generative Adversarial Network; physics guided; 3D field reconstruction; limited measurements

1. Introduction

The gas-solid two-phase flow within fluidized beds effects heat/mass transfer and chemical reaction efficiency, making its hydrodynamic characteristics fundamental to the design and optimization of industrial-scale reactors [1]. Despite significant progress in this field, the inherently complexity of multiphase flows leads to substantial variations in fluidization behavior under different operating conditions and material properties. Existing theoretical models and numerical simulations based on Computational Fluid Dynamics (CFD) remain imperfect [2], frequently relying on simplified assumptions or empirical correlations specific to narrow flow regimes. This limits their universal applicability, and the reliability typically requires experimental validation.

Meanwhile, experimental measurements for fluidized beds are severely challenged. Common intrusive/non-intrusive techniques are constrained due to limited measurement field, restricted operating conditions, and specific requirements for particles, fluids and vessel materials. Consequently, most current methods are restricted to pseudo-2D beds and small pilot units, with few technologies such as pressure measurements, Electrical Capacitance Tomography (ECT), and radioactive particle tracking suitable for industrial applications. The resulting sparse point/surface measurement data impedes in-depth investigation of the complex multiscale dynamic characteristics of fluidized beds.

Pressure measurements are the most prevalent online monitoring tool in industrial plants, owning to their low cost and simplicity. Consequently, identifying flow regimes and evaluating corresponding transfer coefficients from pressure fluctuation curves have been a major focus [1]. However, pressure signals represent spatially averaged sparse data, incapable of revealing flow-field structures. The corresponding interpretation heavily relies on experience, introducing significant uncertainty. Acquiring richer and more precise flow-field details is therefore a critical research objective [3]. Gamma-ray-based particle tracking techniques like Positron Emission Particle Tracking (PEPT) and Radioactive Particle Tracking (RPT) enable detailed in-situ observation of three-dimensional (3D) fluid field in fluidized beds by tracing tracer particles. They show advantages of penetrating metal walls and dense particle beds, alongside tolerance to high temperatures, pressures, and corrosive environments [4], but require strict radiation protection for prolonged operation and suffer from high equipment costs and complex image processing.

Alternatively, based on differences in material permittivity, ECT enables visualization of phase distributions via image reconstruction algorithms. It's no radiation, real-time imaging, low cost, and ease of operation, have led to widespread application. A key limitation, however, is the soft-field nature of electric fields causing image distortion. Significant research efforts focus on correcting sensitivity field distributions, and several methods such as the Landweber iteration method [5] have achieved good results in 2D fields, but distortion remains problematic for 3D systems. Recently, a mobile ECT technique has been developed to measure the sequential 2D cross-sectional data via axial sensor movement. To infer 3D flow fields from these time-varying slices, our prior work introduced a machine learning method known as Fourier Neural Operator (FNO) to synchronization these slices. At any given instant, the phase distribution in one slice is measured by mobile ECT and the others are predicted by pre-trained FNO using experimental data, approximating a 3D field [6]. Nevertheless, the existing inter-slice gaps remain a limitation for hydrodynamic study.

Efficiently extracting meaningful information from limited measurements for detailed 3D field characterization is thus a current research hotspot and challenge. Current research primarily follows two approaches: data fusion and field reconstruction. Data fusion integrates complementary data from diverse sources that describe different characteristics of a complex system to provide a comprehensive view. Liu et al. [7] combined pressure sensors, acoustic transmitters, and ECT to investigate the wetting and drying processes of a spout-fluid bed. Field reconstruction, conversely, aims to generate complete, detailed fields from limited measurements. This inherent requirement for "dimensional upscaling" presents significant challenges for traditional methods but holds potential with Artificial Intelligence (AI) [8].

Recent advances in generative AI techniques have achieved unprecedented success across diverse scientific and engineering domains [9,10]. For the field reconstruction tasks considered in this study, Generative Adversarial Networks (GANs) are a particularly suitable method which employs a generator-discriminator adversarial mechanism to synthesize new pattern-conforming data. Numerous GAN variants have been proposed to extend their generative capacity and tailor performance to specific objectives. Notably, single image GAN (SinGAN) proposed a dedicated multi-scale adversarial training scheme to learn the patch statistics across multiple scales, thus enabled the generation of diverse, realistic samples preserving the original patch distribution [11]. Concurrent-Single-Image GAN (ConSinGAN) further enhanced the efficiency of SinGAN by employing concurrent multi-stage training strategy. The capacity to simultaneously integrate features from different scales enhance the generation of multi-scale structures [12]. This variant has been widely applied to image generation, restoration, and data enhancement [13], and has been successfully applied to couple ECT measurement with electromagnetic tomography (EMT) measurements for enhancing imaging of gas-liquid-solid three-phase flow [14]. Nevertheless, existing GAN variants remain unable to directly handle incomplete measurement data. Due to the absence of detailed training data and physical constraints, the generated outputs often deviate from the true structures and lack physical consistency.

In order to apply to fluidization, the lack of physical realism and mechanistic interpretability of purely data-driven models should be avoided. Alternative approaches, such as Physics-Informed Neural Networks (PINNs) [15] and Physical Encode Neural Networks (PENNs) [16], embed governing equations within their architecture, to ensure adherence to underlying physics. But these methods risk non-convergence when solving complex systems governed by several partial differential equations (PDEs) and struggled to handle inherent uncertainties, which persist in multiphase flow in fluidized beds. Consequently, a strategy integrating physics as guiding constraints, rather than strict governing equations, presents a more suitable path for reconstruction tasks.

To address these challenges, a Physics-guided conditional Generative Adversarial Network (PG-cGAN) approach aims to reconstructing detailed 3D field from incomplete data was proposed in our previous work [17]. The PG-cGAN employs Sequential Gaussian Simulation (SGSIM) [18] to fill missing data regions based on spatial statistics as the initial artifact dataset. The measured data as well as the empirical and semi-empirical correlations

specific to fluidized beds are incorporated as physical constraints, applied to refine the SGSIM-filled data. This integrated strategy enables robust, image restoration-based 3D reconstruction, generating physically plausible structures. This study employs the PG-cGAN method to reconstruct the detailed 3D phase distributions of a fluidized bed from 2D cross-sectional slices obtained via mobile ECT. The computational efficiency and reconstruction accuracy of the generated results were rigorously validated against CFD simulations. Finally, the method was applied to experimental measurement datasets to further analysis of flow characteristics of fluidized beds. The proposed approach provides a paradigm for elucidating complex hydrodynamics in fluidized reactors, offering significant potential for real-time monitoring and optimization of multiphase flow systems.

2. Materials and Methods

2.1. Experimental Setup and Data Acquisition

The experimental setup and data acquisition is illustrated in Figure 1 from our previous work [6]. In the experiments, a cylindrical gas-solid fluid bed was constructed with an inner diameter of 60 mm and a height of 1.0 m, filled with Al_2O_3 particles (Sauter mean diameter 80 μm; density 3900 kg/m^3). Under static conditions, the initial packing height is 0.6 m with solid volume fraction of 0.4. Ambient air is introduced through a porous distributor, yielding a superficial gas velocity of 30.02 mm/s, establishing a bubbling flow regime. The experimentally determined minimum fluidization velocity U_{mf} was found to be 14.5 mm/s.

Measurements are performed using a 16-channel dual ECT sensor. The electrode sheet was attached to the inner side of a slider which is sleeved over the bed. Driven by a servo motor, the slider moves along the axis direction of the bed at a constant speed continuously. The measurement location is controlled at the height of 60, 120, 180, 240, 300, 360, 420, 480, 540 mm from the bottom of the distributor. A total of 5000 frames of ECT slices were recorded at each height, and each slice has a resolution of 64 × 64. Permittivity distributions were reconstructed from raw capacitance data using the Lanweber iteration algorithm [5], with subsequent conversion to normalized concentration distribution using the parallel concentration model. Sensor geometry and signal processing models which have effects on the final results are selected following previous work [19].

Snice concentration distributions at different heights are measured at different times, temporal asynchrony was addressed using a FNO model developed in our earlier study [6]. The FNO model is trained on solid concentration distributions at each individual cross-section for accurate predict the temporal evaluation. During axial traversal, the pre-trained FNO provided real-time estimates of the concentration distribution at other non-measured heights will be predicted in real-time based on the pre-trained FNO model.

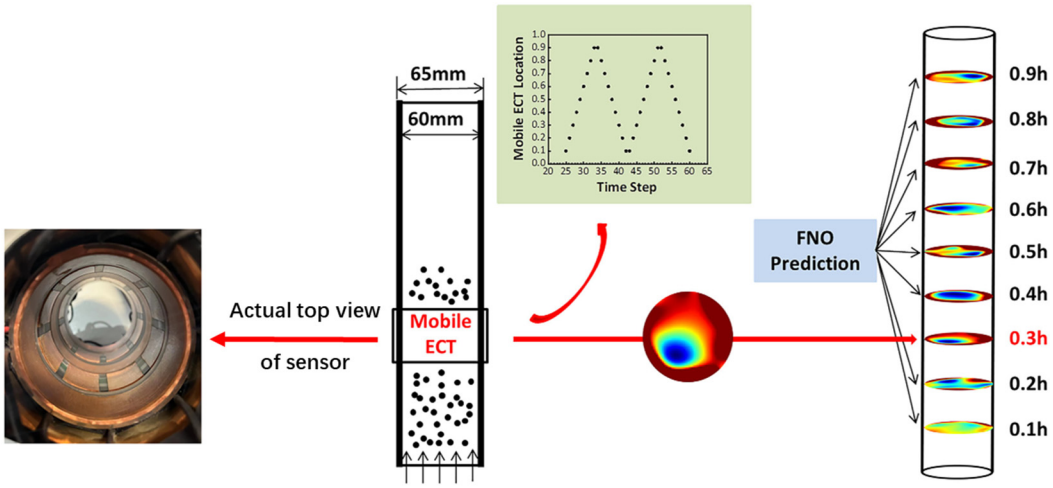

Figure 1. 2D cross-sections measurements of fluidized beds via mobile ECT and FNO prediction [6].

These synchronized 2D concentration slice groups constitute the primary dataset for the comprehensive 3D concentration field reconstruction presented in following.

2.2. Physics Guided cGAN Framework

Based on the aforementioned incomplete measurements, the detailed 3D physical field is generated using a hybrid *Physics guided cGAN* framework. The workflow is shown in Figure 2.

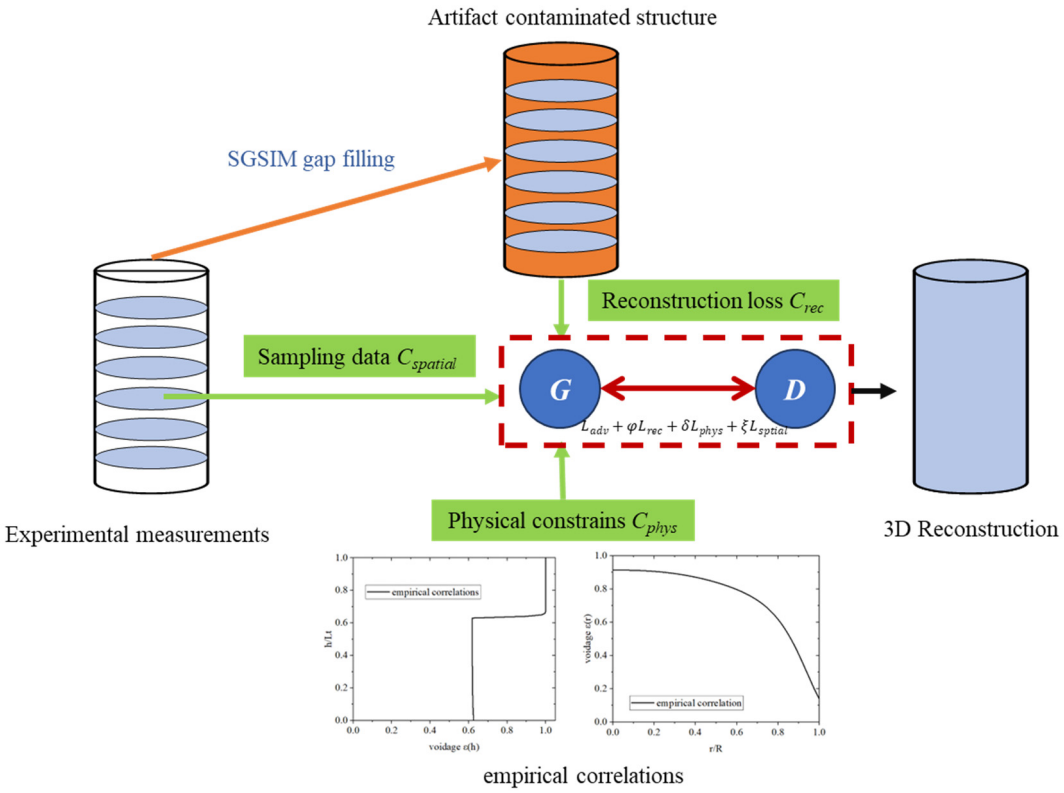

Figure 2. Workflow of the PG-cGAN framework for 3D field reconstruction of in fluidized beds from incomplete measurements.

The core structure of this method is GAN, a deep learning framework that synthesizes realistic data through an adversarial process between two neural networks: a generator G capturing the data distribution of the training data z, denoted as $p_{data}(z)$, and the discriminator D estimating the probability of a sample originating from the training data, denoted as $D(z)$. The training objective is to maximize D's mistaken rate via a minmax game expressed as:

$$\min_G \max_D V(D,G) = \mathbb{E}_{z\sim p_{data}(z)}[log\, D(z)] + \mathbb{E}_{n\sim p_n(n)}[log(1 - D(G(n)))] \quad (1)$$

Here, $G(n)$ denotes the data generated by the generator according to the random noise n with the noise distribution $p_n(n)$ [20]. The concurrent multi-stage training strategy of ConSinGAN, which has the capacity to simultaneously integrate features from different scales is applied for the multiphase flow reconstruction.

Since the original ConSinGAN architecture was designed for 2D image generation, two critical enhancements for reconstructing 3D concentration fields from incomplete 2D slices are implemented:

1. Gap Initialization via SGSIM: The missing data between localized measurements is first estimated using Sequential Gaussian Simulation (SGSIM), with the resulting 3D fields serving as inputs to the adversarial framework.

2. Conditional Physical Constraints: To enhance reconstruction reliability, a conditional modeling architecture is developed to incorporates empirical correlations as physical constraints during the generative process.

2.2.1. SGSIM Gap Filling

SGSIM (Sequential Gaussian Simulation [18]) is a widely method for reconstructing porous media and spatially distributed variables, with applications spanning geology, environmental science, medicine, and related fields. Critically, this method enables full-field reconstruction from sparsely sampled data, that is, effectively performing spatial gap filling. Based on spatial statistical theory and Monte Carlo stochastic theory, SGSIM quantifies the spatial correlation of given data and performs conditional probability reconstruction preserving this correlation as formalized in Equation (2).

$$\gamma(\boldsymbol{h}) = \frac{1}{2}\mathbb{E}[\mathrm{Z}(x_i) - \mathrm{Z}(x_i + \boldsymbol{h})]^2 \quad (2)$$

where $Z(x_i)$ denotes the spatial variables Z at the i^{th} location of the study field $\boldsymbol{x}$, $\boldsymbol{h}$ is the spatial distance between the two variables, and $\gamma(\boldsymbol{h})$ is knowns the variance model.

In the gap filling procedures, SGSIM sequentially visits all gap locations (or unsampled locations) along a random path. At each unsampled location, the conditional mean and variance are computed by kriging method [18] using available data and previously simulated values. A random value is then drawn from this conditional distribution and incorporated into the simulated set. This iterative process continues until all gaps are simulated. While SGSIM demonstrates strong performance for second-order stationarity spatial variables (i.e., those satisfying Equations (3)–(5)), its effectiveness diminishes when handling heterogeneous structures.

$$\mathbb{E}[Z(\boldsymbol{x})] = \mu \tag{3}$$

$$Var[(Z(\boldsymbol{x})] = \frac{1}{N-1}\sum_{i=1}^{N}(Z(x_i) - \mu)^2 = \sigma^2 \tag{4}$$

$$Cov(\boldsymbol{h}) = Cov(x_i, x_i + \boldsymbol{h}) = \mathbb{E}[(Z(x_i) - \mu)(Z(x_i + \boldsymbol{h}) - \mu)] \tag{5}$$

In fluidized bed with a large height-to-diameter ratio in this study, the concentration fields exhibit significant axial and radial distributions. Direct global reconstructions of SGSIM lead to over-homogenization. Under these circumstances, preprocessing of raw data is imperative. In this study, the trend removal method is applied to eliminate spatial inhomogeneity, rendering processed spatial variables compliant with second-order stationarity assumptions suitable for reconstruction, and finally back-transformation is needed to recover the results to original data space. However, good preprocessing needs relative dense sampling data, dependences on domain expertise, and lack of universality hinder its direct application for precise fluidized bed reconstruction. Consequently, this study employs SGSIM merely as a preprocessing step for locally measured data, treating its 3D output as "artifact data" for subsequent refinement and accurate reconstruction via PG-cGAN.

2.2.2. Physics Guided Conditional GAN

In fluidized bed systems, the spatial distribution of gas and solid concentrations represents critical characterization parameters. In order to incorporate the spatial physical information into the generative model, the proposed conditional framework treat spatial coordinates C as conditional inputs, systematically coupling them throughout both generator G and discriminator D networks. The overall architecture is illustrated in Figure 3.

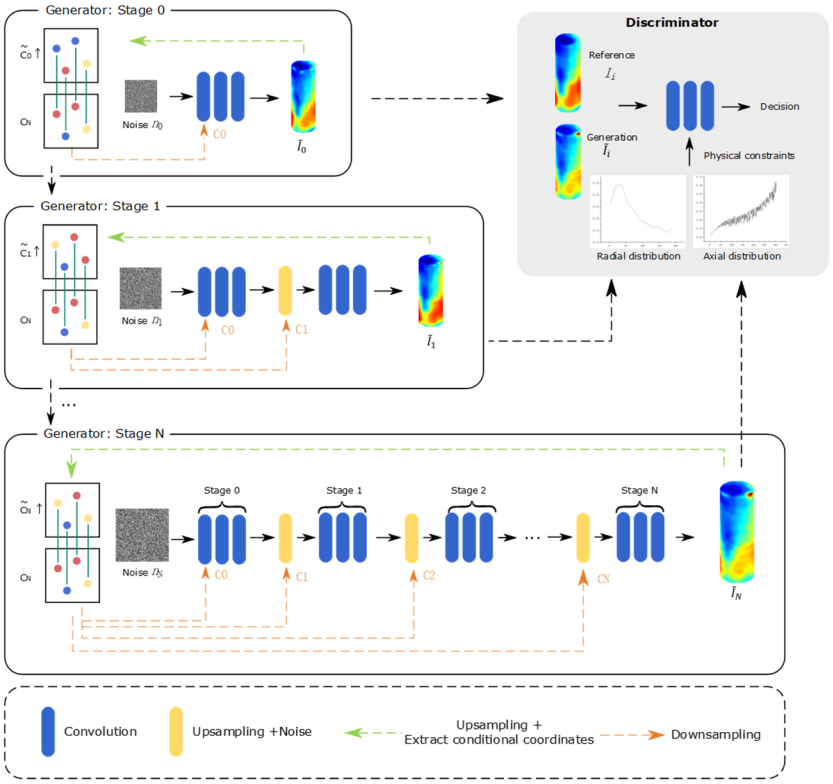

Figure 3. Overview of physics guided conditional ConSinGAN.

Building upon ConSinGAN, the PG- cGAN also employing a multi-layer convolutional network generator to progressively construct images from low to high resolution. At each convolutional layer, both random noise n and the conditional data c_N are simultaneously input, ensuring spatial constraints are maintained across all resolution scales. Here, c_N presenting the corresponding position in the 3D field which is transformed from the coordination C via an embedding encoding layer. And $\tilde{c}_i \uparrow (i = 0,1,\ldots,N)$ denotes upsampled conditional data extracted from the i-th stage. The generator outputs the 3D image $\tilde{I} = G(n, C)$. Then the discriminator takes both the generated image I and spatial coordinates C, and the physical constraints show in Equation (6) and Equation (11) as input, aiming to assess the authenticity of generated images and verify the spatial consistency. The combined loss function for the *i*-th generator-discriminator pair (G_i, D) is formulated combining four key components:

$$\mathcal{L}_{combined}(G_i, D) = \min_{G_i} \max_{D} \mathcal{L}_{adv}(G_i, D) + \varphi \mathcal{L}_{rec}(G_i) + \delta \mathcal{L}_{phys}(G_i) + \xi \mathcal{L}_{spatial}(G_i) \tag{6}$$

where φ, δ and ξ represent the weight coefficients of each loss function. $\mathcal{L}_{adv}(G_i, D)$ represents the adversarial loss that drives the competition between generator and discriminator. To enhance training stability, the Wasserstein distance and gradient penalty term [21] which can mitigate pattern collapse and gradient vanishing are employed in $\mathcal{L}_{adv}(G_i, D)$:

$$\mathcal{L}_{\text{adv}}(G_i, D) = \begin{cases} \underset{\tilde{I}_i \sim P_g}{E}[D(\tilde{I}_i)] - \underset{I_i \sim P_r}{E}[D(I_i)] + \underbrace{\underset{\hat{I}_i \sim P_I}{E}\left[\left(\left\|\nabla_{\hat{I}_i} D(\hat{I}_i)\right\|_2 - 1\right)^2\right]}_{gradient\ penalty} & if\ used\ in\ D \\ -\underset{\tilde{I}_i \sim P_g}{E}[D(\tilde{I}_i)] & if\ used\ in\ G_i \end{cases} \tag{7}$$

where P_g and P_r represent the probability distribution of the generated and real distributions respectively, P_I is the distribution sampled from P_g and P_r, and $\hat{I}_i$ is the variables in image $\tilde{I}_i$ satisfying the distribution P_I. This formulation prevents mode collapse while maintaining stable gradients throughout training. $\mathcal{L}_{rec}(G_i)$ denotes the multi-scale reconstruction loss ensuring feature consistency across resolutions and maintaining the similarity between the generation and reference, expressing as:

$$\mathcal{L}_{rec}(G_i) = \left\|\tilde{I}_i \uparrow - I_i\right\|_2^2 \tag{8}$$

$\mathcal{L}_{spatial}(G_i)$ and $\mathcal{L}_{phys}(G_i)$ are the conditional loss in this proposed model. Since the coordination are conditional inputs in generator, $\mathcal{L}_{spatial}(G_i)$ are defined as Equation (9) to capture the loss maintaining spatial features.

$$\mathcal{L}_{spatial}(G_i) = \|\tilde{c}_i \uparrow - c_N\|_2^2 \tag{9}$$

$\mathcal{L}_{phys}(G_i)$ embodies the physical constraint loss enforcing prior knowledge as:

$$\mathcal{L}_{phys}(G_i) = \left\|F(\tilde{I}_i) - F(I_i)\right\|_2^2 \tag{10}$$

where *F* is the physical constraint function.

Currently, numerous empirical and semi-empirical models have been developed to describe concentration profiles across diverse physical properties and operating conditions. These models not only, enable the evaluation of hydrodynamics and transport coefficient, but also provide validation criteria for both experimental measurements and numerical simulations. In this work, the correlation model match well with our experiments are incorporated as physical constraints within the generative model.

Through systematic analysis of experimental data, we observed that axial gas concentration distribution $\varepsilon(h)$ under our investigation conditions conforms to the bubbling model proposed by Clift and Grace [22], expressed as:

$$\varepsilon(h) = 1 - \frac{1 - \varepsilon_{mf}}{1 + \dfrac{U - U_{mf}}{0.711\sqrt{g d_b(h)}}} \tag{11}$$

where $d_b(h)$ is the bubble size evaluated by the Mori and Wen's model [23] as:

$$d_b(h) = d_{bM} - (d_{bM} - d_{b0}) e^{-0.3h/D_t} \tag{12}$$

$$d_{bM} = 1.87 d_{b0} \tag{13}$$

$$d_{b0} = 0.00376\left[U - U_{mf}\right]^{0.4} \tag{14}$$

And the radial voidage profile $\varepsilon(r)$ match well with the dense bed model proposed by Xu [24]:

$$\varepsilon(r) = \varepsilon_w \left(\frac{\varepsilon_0}{\varepsilon_w}\right)^{F(r)} \tag{15}$$

where

$$\varepsilon_w = \varepsilon_{mf} = 0.48 \tag{16}$$

$$\varepsilon_0 = \varepsilon_{mf} + \frac{1.0 - \varepsilon_{mf}}{0.25}(\bar{\varepsilon} - 0.75) \tag{17}$$

$$F(r) = 1.0 - 0.06\left(\frac{r}{R}\right) - 1.34\left(\frac{r}{R}\right)^2 + 2.65\left(\frac{r}{R}\right)^3 - 2.25\left(\frac{r}{R}\right)^4 \tag{18}$$

with $\bar{\varepsilon}$ presenting the average gas concentration of the study domain. In this study, the measurements data ϕ is the solid-phase concentrations or solid volume fractions, which have the correlation $\phi + \varepsilon = 1$ with gas concentration distribution.

Overall, the inputs of the model consist of three parts: 1. The raw 3D structures generated by SGSIM, which are used as a reference; 2. The ECT measured 2D cross-sections of phase distribution along with their spatial coordinates, which serve as conditional data to reconstruct key flow structures; 3. The empirical axial and radial solid/gas profile models that provides physics guidance to ensure the generated results align with physical processes. Following extensive parameter tuning, both the generator and discriminator consist of an input layer, an output layer, and a convolutional module containing three layers. The 3D convolutional layers (Conv3d) are utilized for 3D coordinates. The input layers utilize 3 input channels, while all the others utilize 64 channels. For more detailed model configuration and parameter sensitivity analysis, readers can refer to our submitted publication focusing on algorithm [17], where comprehensive discussions and tuning guidance are provided. The output of the model is the complete 3D phase-distribution field, which will be discussed in the following section.

3. Results and Discussion

3.1. Validation on Complete CFD Simulations

Based on the experimental conditions, a numerical simulation study was conducted using the Two-Fluid Model (TFM-CFD) with a computational grid of 30 × 250 × 30. More detailed simulation parameters are listed in Table 1. Simulation results from 10 to 20 s with a time step of 0.01 s are used as the dataset. Time-averaged solid-phase concentrations obtained from the numerical simulations were compared with experimental measurements and empirical formula predictions, as shown in Figure 4. Overall, the numerically simulated solid-phase concentrations were slightly higher than the experimental measurements, while the values estimated by the empirical formula were slightly lower. Notably, the empirical formula predicted a radial solid concentration that increased with radial distance, which differed from the experimental observations. In the experimental measurements, a decrease in solid concentration near the wall was observed, particularly at lower bed heights. This phenomenon was also captured in the numerical simulations. These findings demonstrate an agreement among the numerical simulations, empirical formula, and experimental measurements. In this section, the detailed concentration field information obtained from the numerical simulations was utilized to validate the reliability of the proposed method. To enhance computational efficiency, the study region marked by green boxes in Figure 4a, corresponding to the bed section between heights of 6 cm and 54 cm, was selected. This dataset selection is consistent with the experimental measurements.

Table 1. Detailed parameters used in the TFM-CFD simulation.

Property	Setting/value
Gas density (ρ_g)	1.225 kg/m^3
Gas viscosity (μ_g)	1.825×10^{-5} Pa·s
Gas density (ρ_s)	3900 kg/m^3
Solid size (d_p)	80 μm
Drag model	Wen-Yu
Viscous stress model	Algebraic formulation
Frictional stress model	Schaeffer
Outlet boundary condition	Atmospheric pressure
Wall boundary condition	Mixed wall: non-slip for fluid and free-slip for solid
Time step	1×10^{-4} s

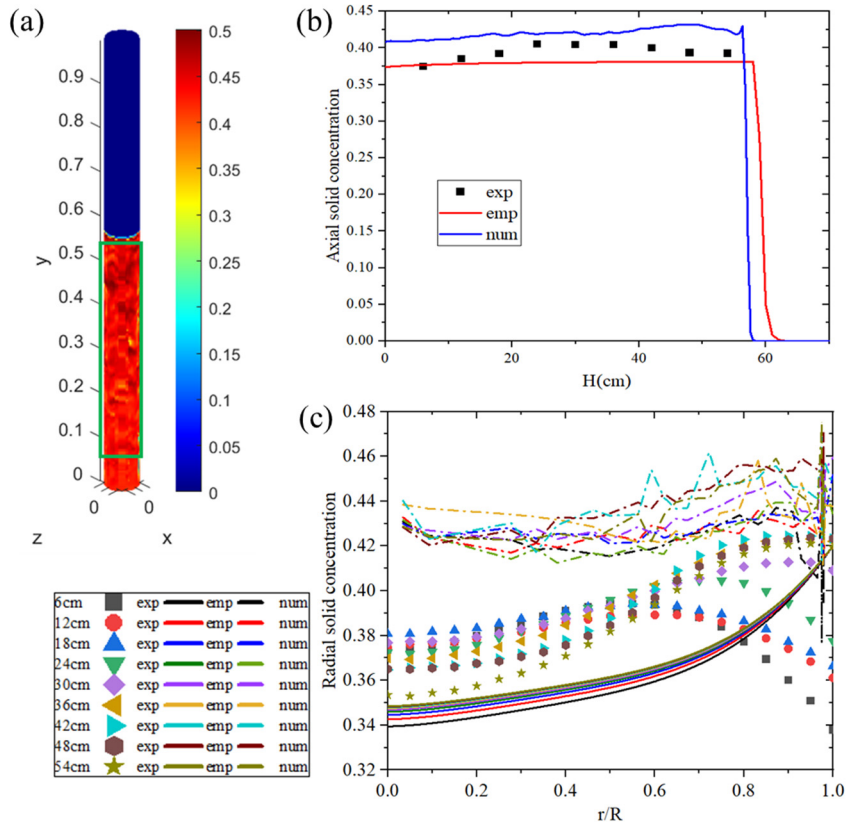

Figure 4. Comparison CFD results with experimental data and empirical correlations: (**a**) CFD simulation results at a single time step; time-averaged solid concentration profiles along (**b**) axial and (**c**) radial directions.

The full 3D solid concentration field from a single CFD transient step is selected as the ground truth or "Real" data for training and comparison. The complete numerical simulation results are first utilized to for reconstruction with and without physics guidance via cGAN. Capitalizing on GANs's capability to generate diverse realizations from training data, reconstructions by cGAN and PG-cGAN are generated. The results and their corresponding error maps from the "Real" are displayed in Figure 5. The error at each location is calculated by:

$$error = \phi_{reconstruction} - \phi_{real} \tag{19}$$

It shows that, the introduction of physical information has a significant impact on the reconstruction results. When physics guidance is not incorporated, the generated output exhibit substantial variations. In contrast, when physics guidance is applied, all reconstructions show strong agreements with the reference simulation field, denoted as "Real" in Figure 5. The error range of each reconstruction generated by the conventional cGAN is inconsistent. Specifically, the first and third examples show a systematic underestimation compared to the "Real" field, The second reconstruction shows errors ranging between −0.15 and 0.15, which are larger than those obtained with PG-cGAN. When physics constraints are considered, the PG-cGAN generated results show a majority of errors range between −0.018 and 0.025, with the maximum error of 0.073.

To further evaluate the generation results, bubble structures were analyzed using a threshold of 0.35. As shown in Figure 6, the reference Real field contains a bubble with an equivalent diameter of 15.8 mm at the height of approximately 0.36 m. With the conditional cGAN method, the position, size, and number of generated bubbles are uncertain, which is the primary source of errors. Due to the systematic underestimation in the first and third cGAN reconstructions, more bubbles are detected using the same threshold. In comparison, while larger deviation primarily occurs in regions with high concentration gradients, the PG-cGAN method successfully preserves essential bubble structural features by incorporating spatial structure and phase distribution information as constraints. Consequently, the bubble positions remain largely unchanged with only minor shape variations, yielding equivalent diameters of 16.2 mm, 15.7 mm, and 16.0 mm, respectively.

Meanwhile, the proposed hybrid cGAN model demonstrates remarkable efficiency. The CFD numerical simulation conducted in this study took approximately 3 days, while the training of the proposed GAN required only about 3.6 h. Once trained, the model can generate other reconstructions in no more than a second. For further details of the performance and effectiveness, please refer to our previously submitted algorithm paper.

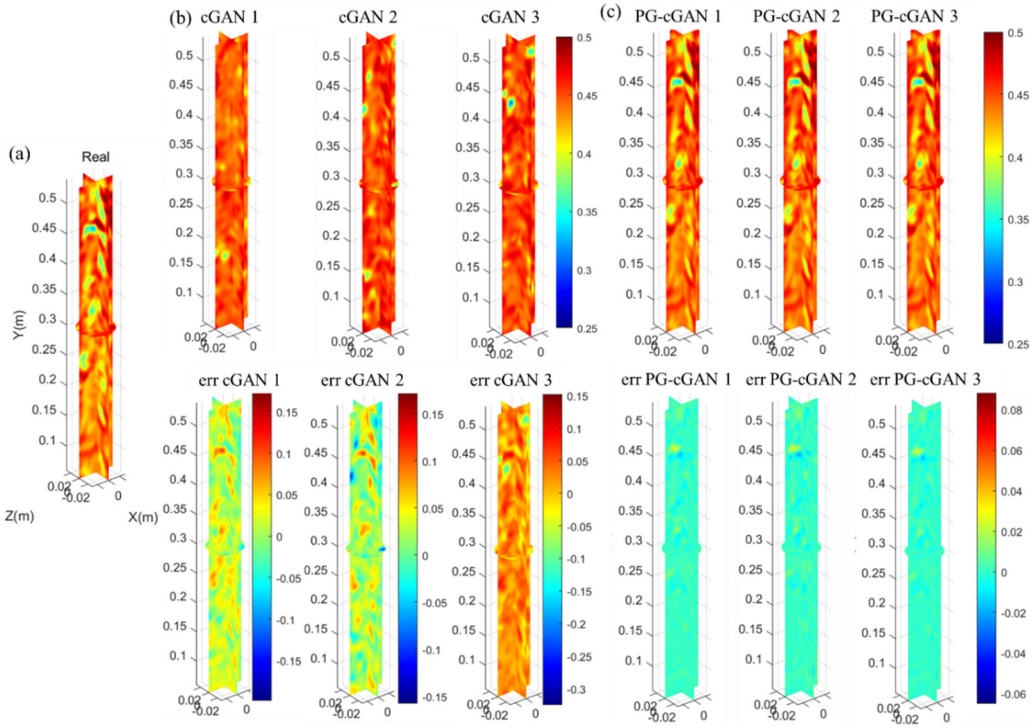

Figure 5. Reconstruction results based on a complete solid concentration field from numerical simulations. (**a**) Real structure; 3 reconstructions and the corresponding errors using (**b**) cGAN without physics-guide and (**c**) PG-cGAN.

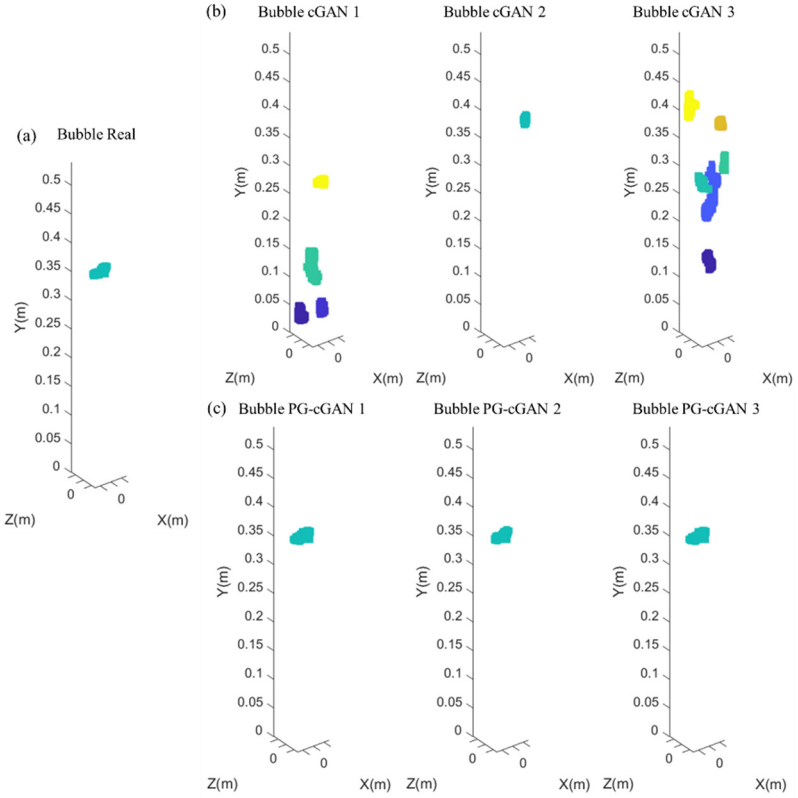

Figure 6. Comparison of typical bubble structures of (**a**) real structure; 3 reconstructions by (**b**) cGAN without physics-guide and (**c**) PG-cGAN.

3.2. Reconstruction Based on Incomplete CFD Simulations

This subsection validates the generation from incomplete data. To adapt to the local measurement, cross-sections are sampled from the full CFD simulation field following the mobile ECT data acquisition principles.

Similarly, using the 3D real data shown in Figure 5 as the benchmark, three samplings with 30 slices, 20 slices and 9 slices are performed. The proposed PG-cGAN method is then implemented based on the sampled data. Figure 7 presents the sampling data, reconstructed results, and their comparative analysis against the real data. It demonstrates that the results generated using both 30 and 20 slices exhibit close agreement with the real field (CFD results). The have comparable error margins and effectively capture key details of the concentration distribution. This alignment is further illustrated in Figure 8, which compares the axial solid concentration profiles.

The results from the denser 30 slices sampling are closer to the real date, the reconstruction from 20 slices also yields close fluctuations. This effectiveness primarily stems from the sampling positions. At this transient time step, two distinct zones with low and rapid changed concentration exist near the height of 0.20 and 0.45 m. These characters are captured by the 20-layer slices, thus contributing to the high quality of the reconstruction results.

For the reconstruction from 9 slices, a degree of averaging presents compared to the true CFD results. The maximum error of 0.12 occurs at the height 0.45 m, where a rapid changed low concentration zone exists but not be sampled. The model failed to generate distinct features at this location due to the absence of relevant input data. At other positions, majority errors remain within the acceptable range of −0.02 to 0.03. Further, the generated solution successfully reproduces the overall axial concentration trend with a reduction in the amplitude of local concentration fluctuations. It is evident that reasonably good results can be generated using 9 layers of data.

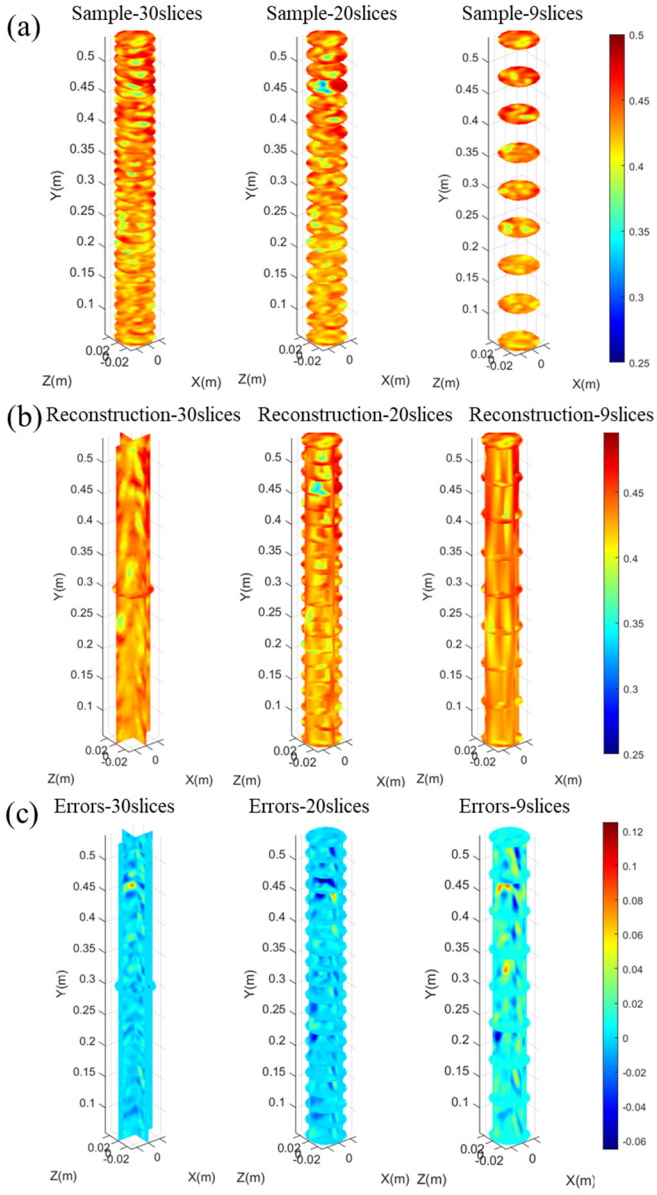

Figure 7. Comparison of reconstruction results obtained from 30, 20, and 9 cross-sectional sampling slices, respectively. (**a**) sampling slices; (**b**) reconstrued structures; (**c**) errors between the reconstruction results and the Real structure.

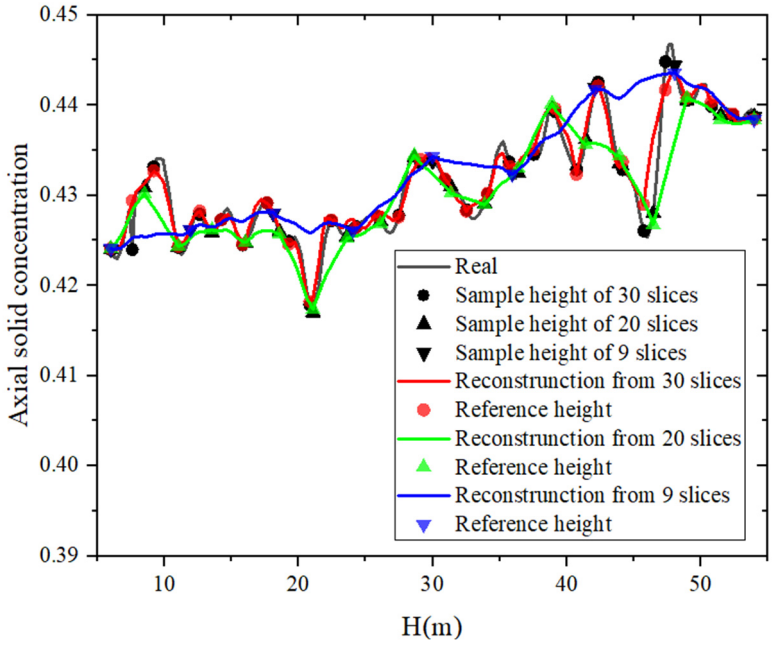

Figure 8. Comparison of axial solid concentration profile of the reconstructions obtained from 30, 20, and 9 cross-sectional sampling slices.

3.3. Reconstruction Based on Mobile ECT Measurements

In this section, the proposed method is applied to mobile ECT measurements. As established earlier, the reconstruction produces consistent results when the cross-sectional data captures critical structural features. Accordingly, the group of measurements presents two bubble-like low-concentration zones at 18 cm and 42 cm bed heights is selected.

The corresponding experimental data and a set of generated reconstruction are presented in Figure 9a. Figure 9b detailed compares the generated results with measurements at each cross-section. The largest errors occur precisely at layers of 18 cm and 42 cm, with error ranges of [−0.05, 0.09] and [−0.03, 0.07], respectively. This observation aligns with the findings in Section 3.2 regarding CFD slice reconstructions: at lower spatial sampling densities, the generated results exhibit averaging effects and struggle to resolve large concentration gradients. At the top and bottom slices, errors fall within [−0.03, 0.04], while errors at intermediate layers are constrained to a narrower range of [−0.02, 0.02]. It comes from the conditional generation strategy employed, which utilizes spatial position as auxiliary input. The top and bottom layers receive less constrained conditioning data compared to intermediate layers, thus exhibiting relatively larger reconstruction errors.

Figure 10 compares the axial solid concentration profiles between the generated and experimental results. In bubbling fluidized beds, the transient concentration distribution exceeds the time-averaged profile across most regions, while falling below the average at bubble locations. The generation model accurately captures this characteristic based on experimental measurements. Significantly, in addition to the low concentration zone at 18 cm height, the reconstruction reveals another low concentration region between 42 cm and 48 cm. This generated structure is likely to be physical present when considering alongside the adjacent measurements at 42 cm and 48 cm, as well as expert empirical knowledge. Using a threshold of 0.35, two bubbles are identified in the reconstruction field: one at a height of 16.2 cm with an equivalent diameter of 3.07 cm, and another at 43.9 cm with an equivalent diameter of 1.46 cm. At the measurement height of 18 cm, the experimentally measured bubble diameter is 3.31 cm, while the cross-sectional diameter of the reconstructed bubble at this cross-section is 3.28 cm. Similarly, at 42 cm, the measured and reconstructed bubble diameters are 1.13 cm 1.11 cm, respectively. The generated results are in good agreement with both experimental measurements and theoretical analysis.

Compared with the results from incomplete CFD presented in Figure 6, the concentration profiles reconstructed from experimental measurements exhibit larger axial fluctuations. This is attributable to the experimental data captures the critical bubble structures, which can be generated by the PG-cGAN model as discussed in Section 3.2. Meanwhile, a finer 64 × 64 grid of the measured cross-sections may provide more information in the generation than that of the 30 × 30 grid in CFD.

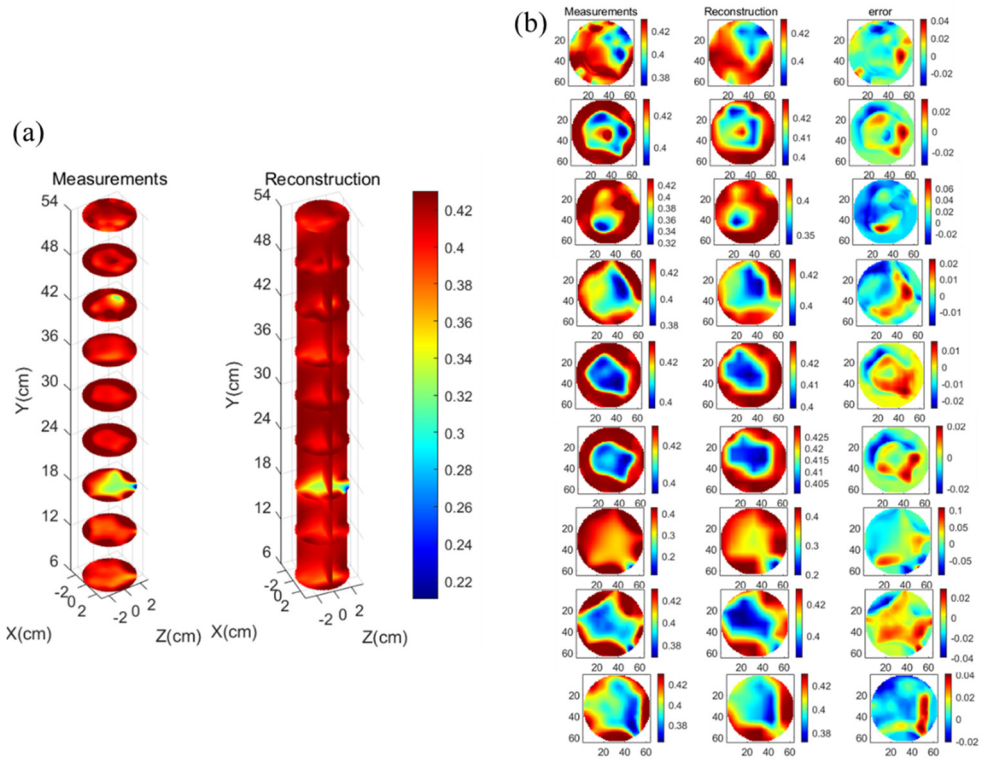

Figure 9. Comparison of reconstruction results based on mobile ECT measurements. (**a**) overview of the reconstruction; and (**b**) detailed comparison at each height.

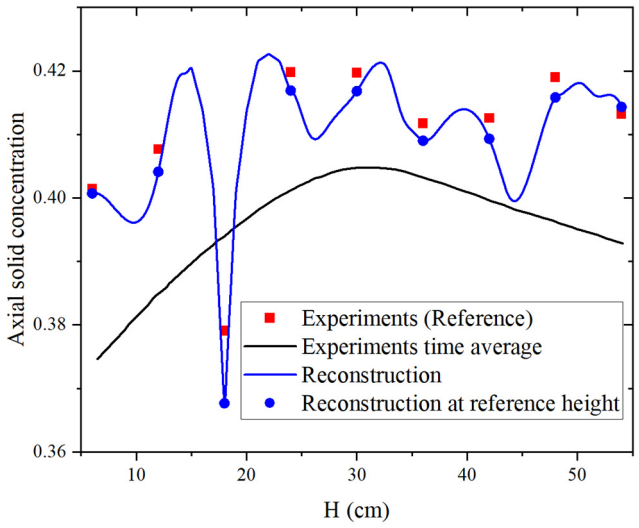

Figure 10. Comparison of axial solid concentration profiles.

4. Conclusions

This study employs a physics guided conditional Generative Adversarial Network (PG-cGAN) to achieve complete 3D field reconstruction from limited data within a fluidized bed. The mobile ECT experiments and CFD-TFM numerical simulations are conducted. Validations based on CFD results demonstrates that the PG-cGAN model has the capability to reconstruct full fields from complete fields with minimal error and significantly higher computational efficiency than CFD. It also successfully reconstructs detailed fields from incomplete data, with reconstruction accuracy directly dependent on the distribution of sampled points. Reconstruction quality improves with denser sampling and better capture of key flow characteristics. Leveraging sparse mobile ECT measurement data, PG-cGAN not only reconstructs complete 3D fields but also predicts potential bubble structure locations from data of adjacent layers, enabling detailed flow field analysis. However, reconstructions from sparse data exhibit an averaging effect. Besides the phase distribution field, this method is capable of reconstructing various spatial structures, such as velocity fields, given corresponding input data. The PG-cGAN shows stochastic nature

that can product diverse outputs from a single input, facilitate error analysis in complex systems with inherent uncertainties, while simultaneously introducing challenges for interpreting the real physical processes. Future research will focus on optimizing sensor placement strategies based on the generated results and exploring more effective methods for incorporating physical information constraints. Moreover, the method can generate different flow structures under various operation conditions by adjusting model parameters. To predict multiple scenarios, a self-adaptive parameter adjustment process is needed, which require further research.

Author Contributions

X.L.: Conceptualization, methodology, visualization, data curation, writing—original draft preparation, resources, funding acquisition; J.X.: investigation, software, data curation, writing—original draft preparation; T.Z.: methodology, investigation, software, data curation, writing—original draft preparation, supervision; C.Z.: investigation, methodology, data curation; A.L.: investigation, methodology, data curation; M.Y.: conceptualization, supervision, project administration, resources, funding acquisition; Z.L.: supervision, project administration, resources. All authors have read and agreed to the published version of the manuscript.

Funding

This work is financially supported by the Strategic Priority Research Program of the Chinese Academy of Sciences (Grant No. XDA0490301), the National Natural Sciences Foundation of China (Grant No. 22108269, 22293024) and the DICP Innovation Foundation (Grant No. I202238).

Institutional Review Board Statement

Not applicable.

Informed Consent Statement

Not applicable.

Data Availability Statement

Data available on request from the authors.

Conflicts of Interest

The authors declare no conflict of interest.

Use of AI and AI-assisted Technologies

No AI tools were utilized for this paper.

References

1. Bi, H.; Grace, J.J. Flow Regime Diagrams for Gas-Solid Fluidization and Upward Transport. *Int. J. Multiph. Flow* **1995**, *21*, 1229–1236.
2. Gidaspow, D. *Multiphase Flow and Fluidization: Continuum and Kinetic Theory Descriptions*; Academic Press: San Diego, CA, USA, 1994.
3. Francia, V.; Wu, K.; Coppens, M.-O. Dynamically Structured Fluidization: Oscillating the Gas Flow and Other Opportunities to Intensify Gas-Solid Fluidized Bed Operation. *Chem. Eng. Process.* **2021**, *159*, 108143.
4. Sykes, J.A.; Weston, D.; Adio, N.; et al. Validation of Simulations of Particulate, Fluid and Multiphase Systems Using Positron Emission Particle Tracking: A Review. *Particuology* **2025**, *101*, 117–145.
5. Yang, W.Q.; Spink, D.M.; York, T.A.; et al. An Image-Reconstruction Algorithm Based on Landweber's Iteration Method for Electrical-Capacitance Tomography. *Meas. Sci. Technol.* **1999**, *10*, 1065–1069.
6. Zhang, C.; Li, A.; Li, C.; et al. Combing Mobile Electrical Capacitance Tomography with Fourier Neural Operator for 3D Fluidized Beds Measurement. *AIChE J.* **2025**, *71*, e18641.
7. Liu, Z.; Wang, H.; Sun, S.; et al. Investigation of Wetting and Drying Process in a Spout-Fluid Bed Using Acoustic Sensor and Electrical Capacitance Tomography. *Chem. Eng. Sci.* **2023**, *281*, 119160.
8. Wang, H.; Fu, T.; Du, Y.; et al. Scientific Discovery in the Age of Artificial Intelligence. *Nature* **2023**, *620*, 47–60.
9. Zeni, C.; Pinsler, R.; Zügner, D.; et al. A Generative Model for Inorganic Materials Design. *Nature* **2025**, *625*, 281–286.

10. Li, Z.; Han, W.; Zhang, Y.; et al. Learning Spatiotemporal Dynamics with a Pretrained Generative Model. *Nat. Mach. Intell.* **2024**, *6*, 1566–1579.
11. Shaham, T.R.; Dekel, T.; Michaeli, T. SinGAN: Learning a Generative Model from a Single Natural Image. *arXiv* **2019**, arXiv:1905.01164.
12. Hinz, T.; Fisher, M.; Wang, O.; et al. Improved Techniques for Training Single-Image GANs. In Proceedings of the 2021 IEEE Winter Conference on Applications of Computer Vision (WACV), Waikoloa, HI, USA, 3–8 January 2021; IEEE: Piscataway, NJ, USA, 2021; pp. 1300–1309.
13. Ouyang, X.; Chen, Y.; Zhu, K.; et al. Image Restoration Refinement with Uformer GAN. In Proceedings of the 2024 IEEE/CVF Conference on Computer Vision and Pattern Recognition Workshops (CVPRW), Seattle, WA, USA, 17–21 June 2024; IEEE: Piscataway, NJ, USA, 2024; pp. 1234–1243.
14. Xia, Z.; Cui, Z.; Chen, Y.; et al. Generative Adversarial Networks for Dual-Modality Electrical Tomography in Multi-Phase Flow Measurement. *Measurement* **2021**, *173*, 108608.
15. Zhang, C.; Li, C.; Li, X.; et al. A General Physics-Informed Neural Network Approach for Deriving Fluid Flow Fields from Temperature Distribution. *Chem. Eng. Sci.* **2025**, *302*, 120950.
16. Rao, C.; Ren, P.; Wang, Q.; et al. Encoding Physics to Learn Reaction–Diffusion Processes. *Nat. Mach. Intell.* **2023**, *5*, 765–779.
17. Zhang, T.; Xiang, J.; Li, X.; et al. 3D Reconstruction of Fluidized Bed Phase Distribution Based on Multi-Scale Conditional Generative Adversarial Network. *Eng. Appl. Artif. Intell.* **2025**, submitted.
18. Bohling, G. GSLIB: Geostatistical Software Library and User's Guide; Computers & Geosciences: Oxford, UK, 1994; pp. 1063–1064.
19. Huang, K.; Meng, S.; Guo, Q.; et al. Effect of Electrode Length of an Electrical Capacitance Tomography Sensor on Gas–Solid Fluidized Bed Measurements. *Ind. Eng. Chem. Res.* **2019**, *58*, 21827–21841.
20. Goodfellow, I.; Pouget-Abadie, J.; Mirza, M.; et al. Generative Adversarial Nets. In *Advances in Neural Information Processing Systems 27*; Ghahramani, Z., Welling, M., Cortes, C., et al., Eds.; Curran Associates: Red Hook, NY, USA, 2014; pp. 2672–2680.
21. Adler, J.; Lunz, S. Banach Wasserstein GAN. In Proceedings of the 32nd International Conference on Neural Information Processing Systems (NeurIPS 2018), Montréal, QC, Canada, 2–8 December 2018; Curran Associates: Red Hook, NY, USA, 2018; pp. 6755–6764.
22. Clift, R.; Grace, J.R. *Continuous Bubbling and Slugging. In Fluidization*, 2nd ed.; Davidson, J.F., Clift, R., Harrison, D., Eds.; Academic Press: London, UK, 1985; pp. 73–131.
23. Mori, S.; Wen, C.Y. Estimation of Bubble Diameter in Gaseous Fluidized Beds. *AIChE J.* **1975**, *21*, 109–115.
24. Xu, G.; Sun, G.; Gao, S. Estimating Radial Voidage Profiles for All Fluidization Regimes in Circulating Fluidized Bed Risers. *Powder Technol.* **2004**, *139*, 186–192.